

# Raman scattering in transition metal dichalcogenides $M\text{Te}_2$ ( $M=\text{Mo}, \text{W}$ )

Xiaoli Ma,<sup>1</sup> Pengjie Guo,<sup>1</sup> Changjing Yi,<sup>2</sup> Qiaohu Yu,<sup>1</sup> Anmin Zhang,<sup>1</sup> Jianting Ji,<sup>1</sup> Yong Tian,<sup>1</sup>  
Feng Jin,<sup>1</sup> YiYan Wang,<sup>1</sup> Kai Liu,<sup>1</sup> Tianlong Xia,<sup>1</sup> Youguo Shi,<sup>2</sup> Qingming Zhang<sup>1,†</sup>

<sup>1</sup>*Department of Physics, Beijing Key Laboratory of Opto-Electronic Functional Materials and Micro-nano Devices, Renmin University of China, Beijing 100872, People's Republic of China*

<sup>2</sup>*Beijing National Laboratory for Condensed Matter Physics, Institute of Physics, Chinese Academy of Sciences, Beijing 100190, People's Republic of China*

## Abstract

We have performed comparable polarized Raman scattering studies of  $\text{MoTe}_2$  and  $\text{WTe}_2$ . By rotating crystals to tune the angle between the principal axis of crystals and the polarization of incident/scattered light, we obtained angle dependence of intensities for all the observed modes, which is perfectly consistent with careful symmetry analysis. Combining this with first-principles calculations, we can clearly identify the observed phonon modes in the different phases of both crystals. Fifteen Raman-active phonon modes ( $10A_g+5B_g$ ) in the high-symmetry phase  $1T'$ - $\text{MoTe}_2$  (300 K) have been well assigned, and all the symmetry-allowed Raman modes ( $11A_1+6A_2$ ) in the low-symmetry phase  $Td$ - $\text{MoTe}_2$  (10 K) and 12 Raman phonons ( $8A_1+4A_2$ ) in  $Td$ - $\text{WTe}_2$  are observed and identified. The present work provides the basic information on lattice dynamics in the transition metal dichalcogenides and may shed some light on the understanding of the extremely large magnetoresistance (MR) in this class of materials.

PACS number(s): 74.70.Xa, 75.47.De, 74.25.Kc, 78.30.-j

---

<sup>†</sup> qmzhang@ruc.edu.cn

## Introduction

Both  $\text{MoTe}_2$  and  $\text{WTe}_2$  are non-magnetic thermoelectric semi-metals [1, 2] discovered in the mid-twentieth century. Recently, it has attracted a great deal of interest in condensed matter physics and material science because of the extremely large MR found in this class of non-magnetic compounds [3-10]. In Td- $\text{WTe}_2$ , for example, it has been experimentally revealed that there exhibits a huge MR at low temperatures when the applied magnetic field and current are along c axis and a axis, respectively. At 0.53 K, the MR under 60 T can reach up to  $1.3 \times 10^7\%$  without saturation trend. Mazhar N. Ali et al. considered that the electron pocket basically has the same size as that of hole pocket [3] at low temperatures in Td- $\text{WTe}_2$ . This has been verified by many experiments like angle-resolved photoemission spectrum (ARPES) [11-13], quantum oscillations [14, 15] and Hall effect [16] experiments. And the experiments under high pressure indicate that the difference between electron and hole pockets increases with increasing pressure, while its MR was gradually suppressed [14]. Therefore, the origin of the huge MR may be attributed to the perfect compensation of electrons and hole pockets [3, 11, 14, 15, 17]. In fact, the mechanism of the extremely large MR is still an open question. In addition, superconducting transition has been observed in Td- $\text{MoTe}_2$  and Td- $\text{WTe}_2$  under pressure [18-20]. For Td- $\text{WTe}_2$ , its  $T_c$  can reach 7K under a pressure of 16.8GPa [18]. And  $T_c$  goes up to 8.2K at  $P = 11.7\text{GPa}$  in Td- $\text{MoTe}_2$  [20]. Interestingly, the very recent studies show that Td- $\text{MoTe}_2$  and Td- $\text{WTe}_2$  are Type-II Weyl semimetals with layered structure [21, 22], whose Weyl point exists at the interface of electron and hole pockets. In fact, most of other layered transition metal chalcogenides (TMDs) like  $\text{MoS}_2$  [23-27] and  $\text{WSe}_2$  [28-31], are semiconductors. This is directly related with their different structures. Generally, various configurations like 2H-, 1T-, 1T'-, Td-structures etc., can be formed in TMDs.  $\text{MoTe}_2$  can exist in the 2H- (hexagonal, space group  $P6_3/mmc$ ), 1T'- (monoclinic, space group  $P2_1/m$ ), or Td-structures (orthorhombic structure, space group  $Pnm2_1$ ) [32]. The 1T'- and Td-structures are quite similar and both of them have a half-metallic state [10, 22]. The symmetry change between the two structures originates from the dislocation between stacked layers [22, 33]. With decreasing temperatures, there occurs a structural transition from monoclinic 1T'-phase to orthogonal Td-phase at  $\sim 270\text{K}$  in  $\text{MoTe}_2$ . The Td-structure of  $\text{MoTe}_2$  is isomorphic with that of  $\text{WTe}_2$  and both of them exhibit a huge MR effect.  $\text{WTe}_2$ , a layered compound with a half-metallic state [1, 3, 35, 36], usually has a stable Td-structure (crystallized to an orthogonal structure of distorted octahedra at atmospheric pressure, space group  $Pnm2_1$ ) [34]. On the other hand, many other TMDs are usually semiconductors with 2H- or 1T-structures. Nowadays  $\text{MoTe}_2/\text{WTe}_2$  and other TMD materials have attracted widespread attentions due to the rich physics such as huge MR effect, superconducting transition under pressure and Weyl semi-metal states etc.

Raman scattering is one of the most conventional and fundamental technique for the study of TMDCs. It can determine the structure and layer number in an easy and nondestructive way [37, 38]. Lattice dynamics study of these materials sets the foundation for exploring possible lattice structures and the influence of phonons on electronic energy band. And it is also a very important basis for the study of  $\text{MoTe}_2$

and WTe<sub>2</sub> heterojunctions, and their doping and phase transitions [2, 39-41].

We conducted a systematic Raman study on MoTe<sub>2</sub> and WTe<sub>2</sub> in this paper. Fifteen Raman-active modes (10A<sub>g</sub>+5B<sub>g</sub>) were measured in 1T'-MoTe<sub>2</sub>. All the 17 A<sub>1</sub>/A<sub>2</sub> mode Raman modes (11A<sub>1</sub>+6A<sub>2</sub>) in Td-MoTe<sub>2</sub> and 12 Raman modes (8A<sub>1</sub>+4A<sub>2</sub>) in Td-WTe<sub>2</sub> were observed, respectively. To resolve the observed phonon modes in MoTe<sub>2</sub> and WTe<sub>2</sub>, we have made polarized Raman measurements. The mode intensity modulations by rotating the samples confirm their symmetries which are in good agreement with strict symmetry analysis. We further carried out first-principle calculation. Combining symmetry analysis and first-principles calculations allow us to clearly identify all the observed modes. And the corresponding vibration patterns were also given.

### Experimental method

Single crystals MTe<sub>2</sub>(M=Mo, W) were grown by a flux method, as described in Ref.14. The polarized and angular Raman spectra were collected with a HR800 spectrometer (Jobin Yvon) equipped with liquid nitrogen cooled CCD and volume Bragg gratings, for which micro-Raman backscattering configuration was adopted. A 633nm laser was used with a spot of ~5 microns focused on sample surface. And the laser power about 1.4 mW was sustained to avoid overheating during measurements.

X/Y in this paper corresponds to a/b axis of crystalline MTe<sub>2</sub> (M = Mo, W). X'/Y' is 45° angle with respect to X/Y. Z is perpendicular to the XY plane. Angle dependence of mode intensity was measured by rotating the crystals and fixing the polarizations of incident and scattered light.

### Calculation method

To determine the phonon modes of WTe<sub>2</sub> and MoTe<sub>2</sub>, first-principle electronic structure calculations were performed with the projector augmented wave method [42] as implemented in the VASP package [43]. For the exchange-correlation potential, the generalized gradient approximation (GGA) of Perdew-Burke-Ernzerh [44] was adopted. To describe the van der Waals (VDW) interaction in layered systems not included in the conventional density functional theory, the vdW-optB86b function [45] was chosen. The kinetic energy cutoff of the plane-wave basis was set to be 300 eV. The simulations were carried out with an orthorhombic supercell containing 4 W atoms and 8 Te atoms. A 20×10×8 k-point mesh was employed for the Brillouin zone sampling. The Gaussian smearing with a width of 0.01 eV was used around the Fermi surface. In structure optimization, both cell parameters and internal atomic positions were allowed to relax until all forces were smaller than 0.005 eV/Å. The calculated lattice parameters are in good agreement with the experimental values (the error is less than 1.7%) [33]. Once the equilibrium structure was obtained, the vibrational frequencies and polarization vectors at Brillouin zone center were calculated using the dynamic matrix method.

## Results and discussions

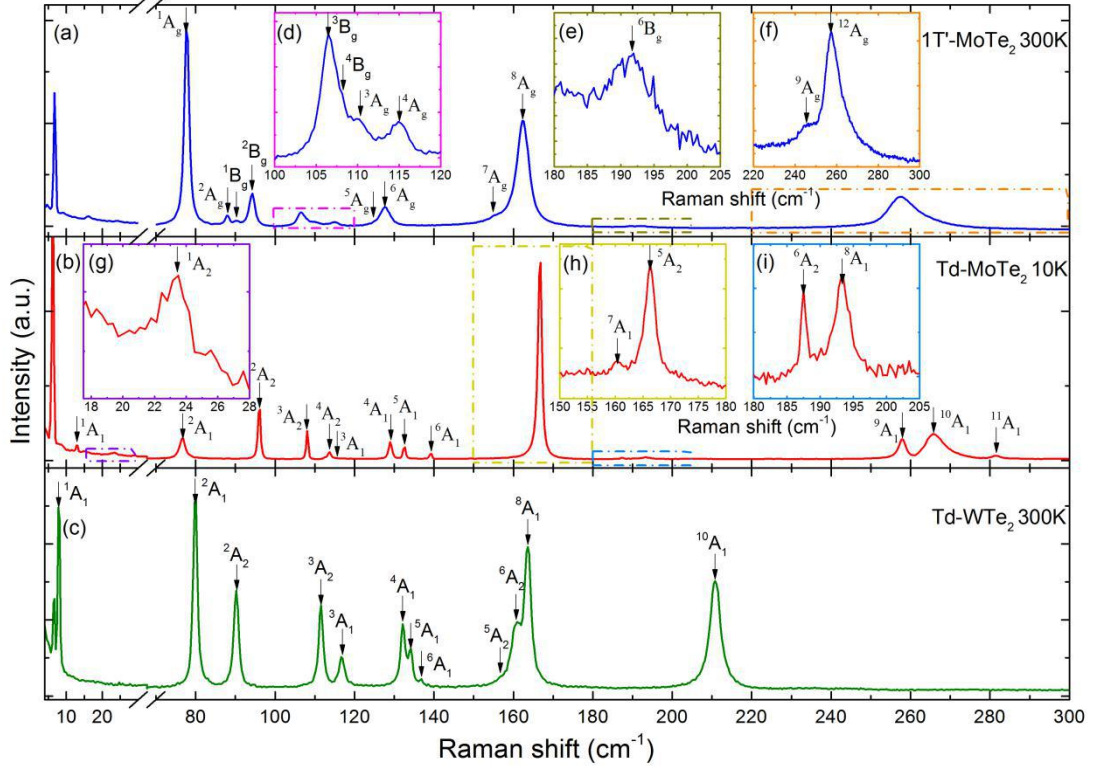


FIG.1. (a) Raman spectrum of 1T'-MoTe<sub>2</sub> measured at 300K. (d), (e) and (f) are zooming in for the modes with weak intensities in (a). (b) Raman spectrum of Td-MoTe<sub>2</sub> measured at 10K. (g), (h) and (i) are zooming in for the modes with weak intensities in (b). (c) Raman spectrum of Td-WTe<sub>2</sub> measured at 10K.

Fig.1 (a) shows Raman spectrum of 1T'-MoTe<sub>2</sub> measured at 300K. 1T'-MoTe<sub>2</sub> has a monoclinic structure with space group  $P2_1/m(C_{2h})$  [32, 34], which allows 18 Raman active phonon modes (12 A<sub>g</sub> modes and 6 B<sub>g</sub> modes). These modes should be visible when the incident light vertically hits on ab plane. In fact, we observed 15 Raman-active phonon modes. The other three modes are invisible, perhaps due to weak signal. The signal at the lowest frequencies comes from laser line. Fig.1 (b), (c) are the spectrum of Td-MoTe<sub>2</sub> measured at 10K and the spectrum of Td-WTe<sub>2</sub> measured at 300K, respectively. Td-MoTe<sub>2</sub> and Td-WTe<sub>2</sub> have the same orthorhombic structure with space group  $Pnm2_1(C_{7v}^2)$  [46]. Symmetry analysis indicates that there should be 33 Raman active phonon modes [11A<sub>1</sub>+6A<sub>2</sub>+5B<sub>1</sub>+11B<sub>2</sub>] in the low-symmetry phase. Our measurements were conducted on ab plane. This allows 17 Raman modes (11A<sub>1</sub> + 6A<sub>2</sub>). All the 17 modes in Td-MoTe<sub>2</sub> have been observed. Comparably, only 12 Raman modes in Td-WTe<sub>2</sub> were observed under the same experimental conditions. The reason may be simply attributed to the weak signal for the other five invisible phonon modes. Just like in 1T'-MoTe<sub>2</sub> (Fig. 1(a)), the peak at the lowest frequencies in Td-MoTe<sub>2</sub> (Fig. 1(b)) also comes from excitation laser spectrum, while the peaks at the lowest frequencies in Td-WTe<sub>2</sub> (Fig. 1(c)) actually contain laser line plus a phonon mode. To verify the symmetry of the observed modes, we further measured polarized Raman spectra.

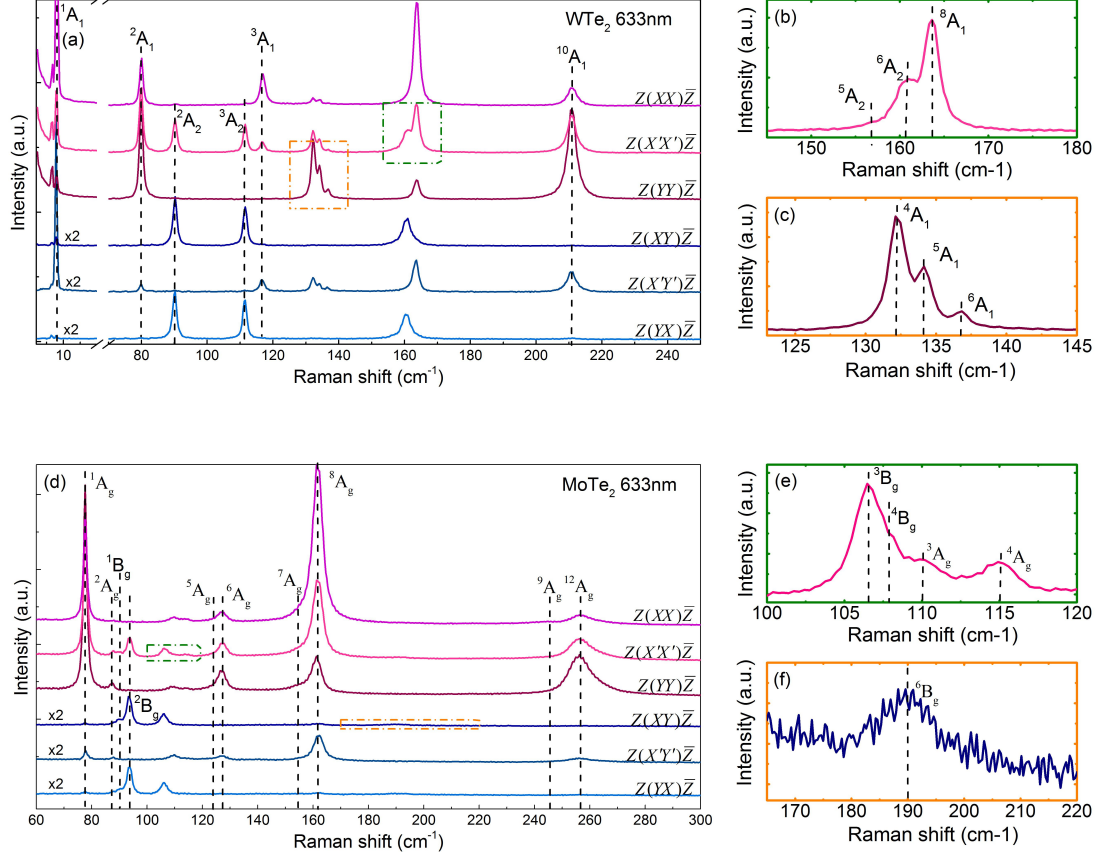


FIG. 2. (a) Polarized Raman spectrum of Td-WTe<sub>2</sub> measured at room temperature with a 633 nm laser. (b)&(c) A zoom-in view of the green/orange dotted box in Fig. 2(a). (d) Polarized Raman spectrum of 1T'-MoTe<sub>2</sub> measured at room temperature with a 633 nm laser. (e)&(f) A zoom-in view of the green/orange dotted box in Fig. 2(d).

Fig. 2 shows polarized Raman spectra of Td-WTe<sub>2</sub> and 1T'-MoTe<sub>2</sub> at room temperature under different polarization configurations. 12 and 15 Raman modes can be seen in Td-WTe<sub>2</sub> and 1T'-MoTe<sub>2</sub>, respectively. The comparison between the spectra of the two similar structures demonstrates that the subtle structural difference can be clearly distinguished by Raman scattering.

Bulk Td-WTe<sub>2</sub> has an orthogonal structure with space group Pnm2<sub>1</sub>(C<sub>72v</sub>) [46], in which layers are stacked along c-axis. Generally, Raman intensities are determined by Raman tensors. Raman tensors for WTe<sub>2</sub> are the following:

$$A_1 = \begin{pmatrix} a & 0 & 0 \\ 0 & b & 0 \\ 0 & 0 & c \end{pmatrix}, \quad A_2 = \begin{pmatrix} 0 & d & 0 \\ d & 0 & 0 \\ 0 & 0 & 0 \end{pmatrix}, \quad B_1 = \begin{pmatrix} 0 & 0 & e \\ 0 & 0 & 0 \\ e & 0 & 0 \end{pmatrix}, \quad B_2 = \begin{pmatrix} 0 & 0 & 0 \\ 0 & 0 & f \\ 0 & f & 0 \end{pmatrix}$$

Symmetry analysis indicates that only A<sub>1</sub> and A<sub>2</sub> modes are visible in our case, since our measurements were made on ab plane. According to the tensors of A<sub>1</sub> and A<sub>2</sub> modes, all of the 12 Raman modes can be seen in the channel of Z(X'X')Z-bar

( $e_i // e_s, \theta = 45^\circ$ ) or  $Z(X'Y')\bar{Z}$  ( $e_i \perp e_s, \theta = 45^\circ$ ), while in  $Z(XX)\bar{Z}$  ( $e_i // e_s, \theta = 0^\circ$ ) or  $Z(YY)\bar{Z}$  ( $e_i // e_s, \theta = 90^\circ$ ), only 8  $A_1$  modes should be seen. Experimentally they are located at  $8.0 \text{ cm}^{-1}(^1A_1)$ ,  $80.1 \text{ cm}^{-1}(^2A_1)$ ,  $117.7 \text{ cm}^{-1}(^3A_1)$ ,  $132.9 \text{ cm}^{-1}(^4A_1)$ ,  $134.8 \text{ cm}^{-1}(^5A_1)$ ,  $138.4 \text{ cm}^{-1}(^6A_1)$ ,  $164.5 \text{ cm}^{-1}(^8A_1)$ ,  $212.0 \text{ cm}^{-1}(^9A_1)$ . In  $Z(XY)\bar{Z}$  ( $e_i \perp e_s, \theta = 0^\circ$ ) or  $Z(YX)\bar{Z}$  ( $e_i \perp e_s, \theta = 90^\circ$ ), only four  $A_2$  modes are visible and located at  $90.6 \text{ cm}^{-1}(^2A_2)$ ,  $112.1 \text{ cm}^{-1}(^3A_2)$ ,  $156.1 \text{ cm}^{-1}(^5A_2)$ ,  $161.2 \text{ cm}^{-1}(^6A_2)$ , respectively. Through careful polarized Raman measurements, we can easily distinguish  $A_1$  and  $A_2$  modes.

On the other hand, bulk 1T'-MoTe<sub>2</sub> has a monoclinic structure with space group  $P2_1/m(C_{2h})$  [32, 34]. Its Raman tensors are written as:

$$A_g = \begin{pmatrix} b & 0 & d \\ 0 & c & 0 \\ d & 0 & a \end{pmatrix}, \quad B_g = \begin{pmatrix} 0 & f & 0 \\ f & 0 & e \\ 0 & e & 0 \end{pmatrix},$$

Symmetry analysis tells us that  $A_g$  and  $B_g$  modes are visible when the measurements are made on ab plane. The tensors of  $A_g$  and  $B_g$  modes allow 15 Raman modes in  $Z(X'X')\bar{Z}$  ( $e_i // e_s, \theta = 45^\circ$ ) or  $Z(X'Y')\bar{Z}$  ( $e_i \perp e_s, \theta = 45^\circ$ ), and all of them have been observed. Only 10  $A_g$  modes can be seen in  $Z(XX)\bar{Z}$  ( $e_i // e_s, \theta = 0^\circ$ ) or  $Z(YY)\bar{Z}$  ( $e_i // e_s, \theta = 90^\circ$ ). Experimentally they correspond to  $77.0 \text{ cm}^{-1}(^1A_g)$ ,  $86.3 \text{ cm}^{-1}(^2A_g)$ ,  $110.7 \text{ cm}^{-1}(^3A_g)$ ,  $114.5 \text{ cm}^{-1}(^4A_g)$ ,  $127.8 \text{ cm}^{-1}(^5A_g)$ ,  $129.0 \text{ cm}^{-1}(^6A_g)$ ,  $155.4 \text{ cm}^{-1}(^7A_g)$ ,  $163.3 \text{ cm}^{-1}(^8A_g)$ ,  $245.0 \text{ cm}^{-1}(^9A_g)$ ,  $256.3 \text{ cm}^{-1}(^{12}A_g)$ . And in  $Z(XY)\bar{Z}$  ( $e_i \perp e_s, \theta = 0^\circ$ ) or  $Z(YX)\bar{Z}$  ( $e_i \perp e_s, \theta = 90^\circ$ ), only five  $B_g$  modes should be seen, corresponding to  $91.2 \text{ cm}^{-1}(^1B_g)$ ,  $94.4 \text{ cm}^{-1}(^2B_g)$ ,  $106.1 \text{ cm}^{-1}(^3B_g)$ ,  $107.0 \text{ cm}^{-1}(^4B_g)$ ,  $191.2 \text{ cm}^{-1}(^6B_g)$ , respectively. Therefore, one can select out  $A_g$  or  $B_g$  modes by different polarization configurations.

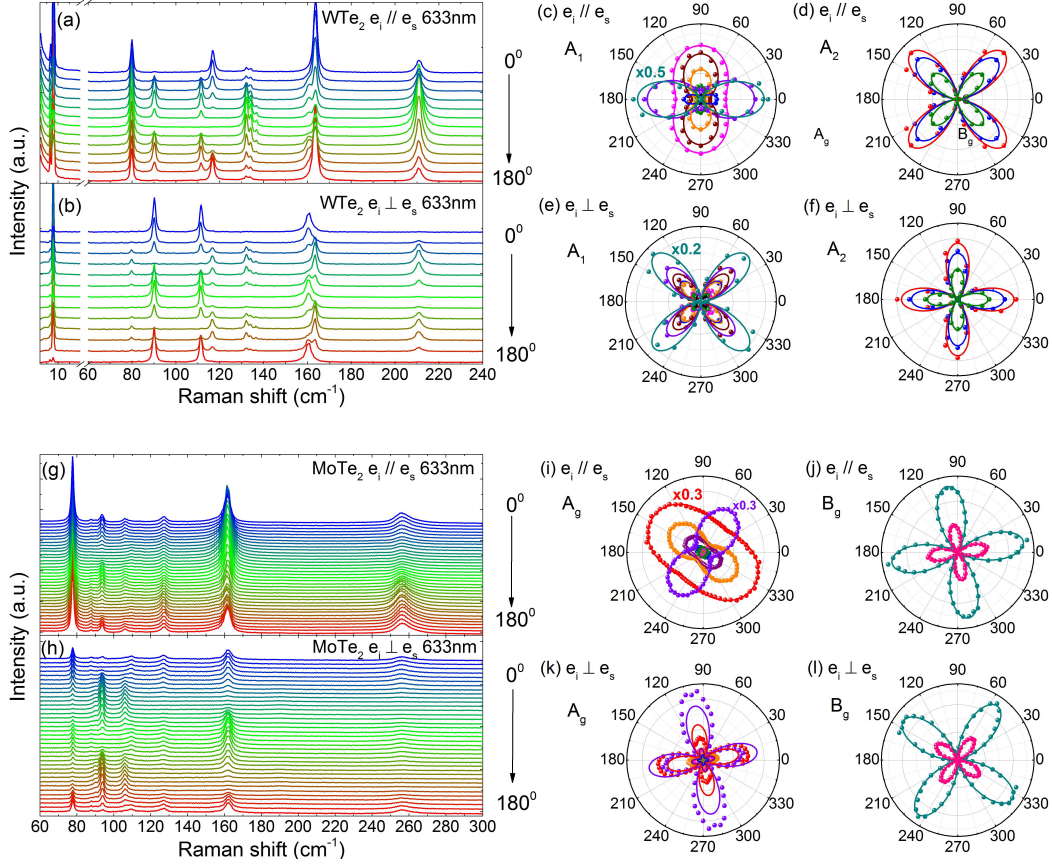


FIG. 3. (a) and (b) Angle dependence of Td-WTe<sub>2</sub> in parallel and cross polarization configurations. (g) & (h) Angle dependence of 1T'-MoTe<sub>2</sub> in parallel and cross polarization configurations. (c)-(f) Intensity plots with respect to rotation angle for A<sub>1</sub>/A<sub>2</sub> modes of Td-WTe<sub>2</sub>. (i)-(l) Intensity plots with respect to rotation angle for A<sub>g</sub>/B<sub>g</sub> modes of 1T'-MoTe<sub>2</sub>.

Fig.3(a)&(b)/(g)&(h) show angle dependence of Raman intensities for Td-WTe<sub>2</sub>/1T'-MoTe<sub>2</sub> in both parallel and cross channels. It can be seen that Raman intensities exhibit a regular change with rotating crystals. And the intensity variations have been illustratively summarized in Fig.3(c)-(f)/(i)-(l). Here  $e_i$  and  $e_s$  are the polarizations of incident and scattered light, respectively. And the angle between the polarizations of the incident light and the principal axis (axis a) is defined as  $\theta$ . According to the above Raman tensors, Raman intensities for different symmetries in Td-WTe<sub>2</sub> can be written as:

$$e_i // e_s: A_1: I = [b + (a - b) \cos^2 \theta]^2 \quad (1)$$

$$A_2: I = (d \sin 2\theta)^2 \quad (2)$$

$$e_i \perp e_s: A_1: I = \left( \frac{b - a}{2} \sin 2\theta \right)^2 \quad (3)$$

$$A_2: I = (d \cos 2\theta)^2 \quad (4)$$

Similarly, Raman intensities for different symmetries in 1T'-MoTe<sub>2</sub> have the following forms:

$$e_i // e_s: A_g: I = [c + (b - c) \cos^2 \theta]^2 \quad (5)$$

$$B_g: I = (f \sin 2\theta)^2 \quad (6)$$

$$e_i \perp e_s: A_g: I = \left( \frac{c - b}{2} \sin 2\theta \right)^2 \quad (7)$$

$$B_g: I = (f \cos 2\theta)^2 \quad (8)$$

Though the both structures are closely similar, polarized Raman measurements can tell the subtle dependencies. The angle dependence for A<sub>1</sub>(A<sub>g</sub>) modes in the parallel channel has twofold symmetry, while it is fourfold symmetry for A<sub>2</sub>(B<sub>g</sub>) modes. The angle dependence for A<sub>1</sub>/A<sub>2</sub> and A<sub>g</sub>/B<sub>g</sub> modes in cross channel has fourfold symmetry, but the maximum intensities appear in different angles, depending on mode symmetries. It should be noted that the non-zero starting angle of 1T'-MoTe<sub>2</sub> has been taken into account. From Fig. 3 (c)-(f), (i)-(l), we found that the detailed symmetry analysis is well consistent with the experiments. This indicates that the symmetry identification for each phonon in Td-WTe<sub>2</sub> and 1T'-MoTe<sub>2</sub> is reasonable.

To assign the observed modes, we have further performed first-principles calculations. The experimental and calculated mode frequencies are summarized in Table 1. The table indicates that the experimental values agree with the calculated data quite well. Totally there are 11A<sub>1</sub>+6A<sub>2</sub>+5B<sub>1</sub>+11B<sub>2</sub> vibration modes in Td-MoTe<sub>2</sub>/Td-WTe<sub>2</sub>. Among them, six A<sub>2</sub> modes are Raman active and the rest are infrared and Raman active. 12A<sub>g</sub>+6B<sub>g</sub>+5A<sub>u</sub>+10B<sub>u</sub> vibration modes are allowed in 1T'-MoTe<sub>2</sub>. 12 A<sub>g</sub> mode and 6 B<sub>g</sub> modes are Raman-active and the rest 5 A<sub>u</sub> modes and 10 B<sub>u</sub> modes are infrared active.

TABLE I. Comparison of the calculated and experimental optical phonon modes (in  $\text{cm}^{-1}$ ) for Td-MoTe<sub>2</sub>/Td-WTe<sub>2</sub> and 1T'-MoTe<sub>2</sub>. The main atomic motions of the modes are also given (see Fig.4). *I* and *R* denote infrared and Raman activities, respectively.

Td-MoTe <sub>2</sub> / Td-WTe <sub>2</sub>				1T'-MoTe <sub>2</sub>			
Symmetry	Calculation	Experiment	Activity	Symmetry	Calculation	Experiment	Activity
<sup>1</sup> A <sub>1</sub>	10.3 / 9.5	13.0 / 8.0	I+R	<sup>1</sup> B <sub>u</sub>	8.8		I
<sup>1</sup> A <sub>2</sub>	26.9 / 24.3	23.6	R	<sup>1</sup> A <sub>u</sub>	26.3		I
<sup>1</sup> B <sub>2</sub>	32.1 / 28.2		I+R	<sup>2</sup> B <sub>u</sub>	32.5		I
<sup>2</sup> A <sub>1</sub>	77.4 / 76.2	76.7 / 80.1	I+R	<sup>1</sup> A <sub>g</sub>	76.6	77.0	R
<sup>2</sup> B <sub>2</sub>	85.8 / 86.1		I+R	<sup>2</sup> A <sub>g</sub>	84.8	86.3	R
<sup>1</sup> B <sub>1</sub>	88.5 / 87.1		I+R	<sup>1</sup> B <sub>g</sub>	88.2	91.2	R
<sup>2</sup> A <sub>2</sub>	91.2 / 88.1	96.1 / 90.6	R	<sup>2</sup> B <sub>g</sub>	91.0	94.4	R
<sup>3</sup> A <sub>2</sub>	104.6 / 109.7	108.1 / 112.1	R	<sup>3</sup> B <sub>g</sub>	104.0	106.1	R
<sup>2</sup> B <sub>1</sub>	105.3 / 110.0		I+R	<sup>4</sup> B <sub>g</sub>	104.7	107.0	R
<sup>4</sup> A <sub>2</sub>	108.0 / 113.0	113.7	R	<sup>2</sup> A <sub>u</sub>	107.9		I
<sup>3</sup> A <sub>1</sub>	108.7 / 113.2	115.5 / 117.7	I+R	<sup>3</sup> A <sub>g</sub>	109.4	110.7	R
<sup>3</sup> B <sub>1</sub>	110.6 / 115.2		I+R	<sup>3</sup> A <sub>u</sub>	110.4		I
<sup>3</sup> B <sub>2</sub>	113.0 / 117.6		I+R	<sup>4</sup> A <sub>g</sub>	113.6	114.5	R
<sup>4</sup> B <sub>2</sub>	115.1 / 123.0		I+R	<sup>3</sup> B <sub>u</sub>	116.0		I
<sup>4</sup> A <sub>1</sub>	122.4 / 128.5	129.1 / 132.9	I+R	<sup>4</sup> B <sub>u</sub>	123.4		I
<sup>5</sup> A <sub>1</sub>	125.1 / 130.6	132.6 / 134.8	I+R	<sup>5</sup> A <sub>g</sub>	125.5	127.8	R
<sup>5</sup> B <sub>2</sub>	127.3 / 132.3		I+R	<sup>6</sup> A <sub>g</sub>	127.0	129.0	R
<sup>6</sup> B <sub>2</sub>	128.9 / 127.4		I+R	<sup>5</sup> B <sub>u</sub>	129.0		I
<sup>6</sup> A <sub>1</sub>	134.2 / 132.0	139.2 / 138.4	I+R	<sup>6</sup> B <sub>u</sub>	133.9		I
<sup>7</sup> B <sub>2</sub>	153.7 / 154.8		I+R	<sup>7</sup> A <sub>g</sub>	153.2	155.4	R
<sup>7</sup> A <sub>1</sub>	158.6 / 158.8	160.4	I+R	<sup>8</sup> A <sub>g</sub>	158.5	163.3	R
<sup>5</sup> A <sub>2</sub>	175.9 / 151.0	166.7 / 156.1	R	<sup>4</sup> A <sub>u</sub>	175.5		I
<sup>4</sup> B <sub>1</sub>	176.3 / 151.2		I+R	<sup>5</sup> A <sub>u</sub>	176.2		I
<sup>6</sup> A <sub>2</sub>	188.4 / 159.5	187.5 / 161.2	R	<sup>5</sup> B <sub>g</sub>	186.9		R
<sup>5</sup> B <sub>1</sub>	188.9 / 161.0		I+R	<sup>6</sup> B <sub>g</sub>	187.9	191.2	R
<sup>8</sup> A <sub>1</sub>	191.2 / 171.9	193.3 / 164.5	I+R	<sup>7</sup> B <sub>u</sub>	190.8		I
<sup>8</sup> B <sub>2</sub>	191.4 / 170.7		I+R	<sup>8</sup> B <sub>u</sub>	191.6		I
<sup>9</sup> A <sub>1</sub>	244.9 / 209.1	258.1 / 212.0	I+R	<sup>9</sup> A <sub>g</sub>	242.0	245.0	R
<sup>9</sup> B <sub>2</sub>	245.6 / 210.6		I+R	<sup>10</sup> A <sub>g</sub>	246.8		R
<sup>10</sup> B <sub>2</sub>	251.6 / 205.8		I+R	<sup>11</sup> A <sub>g</sub>	252.4		R
<sup>10</sup> A <sub>1</sub>	251.6 / 205.6	265.4	I+R	<sup>12</sup> A <sub>g</sub>	254.9	256.3	R
<sup>11</sup> B <sub>2</sub>	265.1 / 231.7		I+R	<sup>9</sup> B <sub>u</sub>	266.6		I
<sup>11</sup> A <sub>1</sub>	265.9 / 231.2	280.4	I+R	<sup>10</sup> B <sub>u</sub>	267.3		I

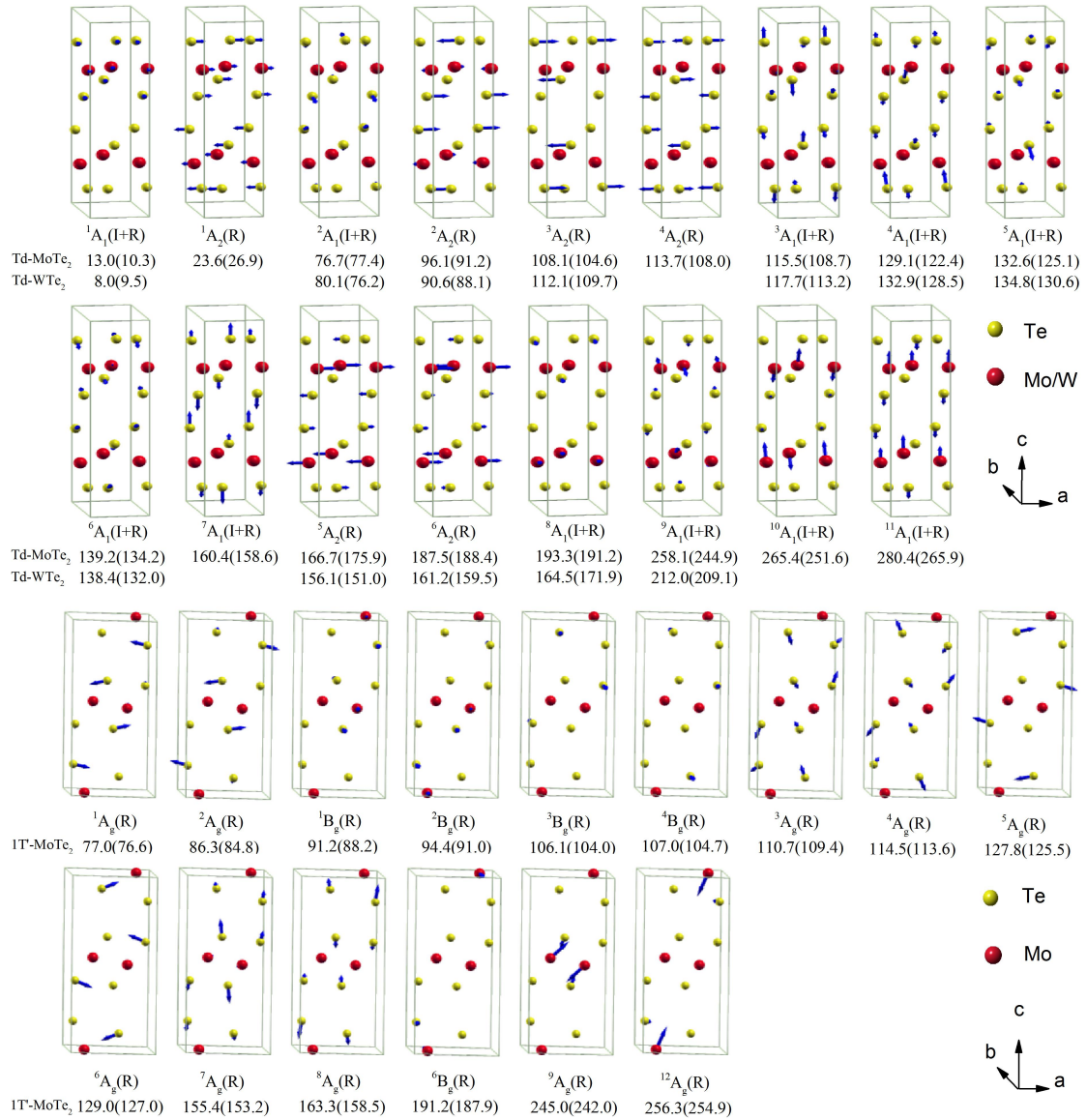


FIG.4. Vibration patterns of all the Raman modes observed in Td-MoTe<sub>2</sub>/Td-WTe<sub>2</sub> and 1T'-MoTe<sub>2</sub>. The mode symmetry, optical activity and experimental (calculated) phonon frequency are also listed below each pattern. I/R represents infrared/Raman activity.

The vibration patterns of the observed phonon modes are illustrated in Fig.4. Td-WTe<sub>2</sub> and Td-MoTe<sub>2</sub> have the same structure and the identical vibration patterns. The first two rows of Fig. 4 show the vibration patterns of Td-WTe<sub>2</sub> and Td-MoTe<sub>2</sub>. Since the effective mass  $m$  of W is larger than Mo and  $\omega \propto \sqrt{k/m}$ , phonon frequency  $\omega$  of Td-WTe<sub>2</sub> is expected to be smaller than that of Td-MoTe<sub>2</sub> for the same mode. The calculations indicate that most of the modes follow this expectation. But a few phonon modes look relatively anomalous and this may be caused by the change of the relevant spring constants. Meanwhile, the experimental data are consistent with the calculations and this may support the above speculation. The last two rows of Fig. 4 show vibration patterns of 1T'-MoTe<sub>2</sub>. The phase transition from

1T'-phase to Td-phase in MoTe<sub>2</sub> is correlated with the stacked misalignment between the layers. If Comparing the interlayer modes of 1T'-MoTe<sub>2</sub> (e.g. <sup>7</sup>A<sub>g</sub>) with those of Td-MoTe<sub>2</sub> (e.g. <sup>7</sup>A<sub>1</sub>), one can find that the corresponding vibration patterns have just small changes across the phase transition. This suggests that the phase transition little affects on the interlayer modes.

## Conclusion

This paper gives a comprehensive identification of vibration modes for 1T'-MoTe<sub>2</sub>, Td-MoTe<sub>2</sub> and Td-WTe<sub>2</sub>. Polarized Raman spectra of bulk 1T'-MoTe<sub>2</sub>, Td-MoTe<sub>2</sub> and Td-WTe<sub>2</sub> were measured and 15, 17 and 12 Raman-active phonon modes were observed, respectively. The A<sub>1</sub>(A<sub>g</sub>) and A<sub>2</sub>(B<sub>g</sub>) modes were distinguished by careful polarized measurements combined with group theory analysis. First-principles calculations have been conducted to identify vibration pattern for each mode. By comparing the vibration patterns of the interlayer modes of 1T'-MoTe<sub>2</sub> and Td-MoTe<sub>2</sub>, the phase transition was found to have very small impact on the interlayer modes. These may have a very important meaning for the studies of MoTe<sub>2</sub> and WTe<sub>2</sub> heterojunctions, doping, and phase transition etc.

## Acknowledgment

This work was supported by the Ministry of Science and Technology of China (Grant No.: 2016YFA0300504) and the NSF of China Y.G.S was supported by the Strategic Priority Research Program (B) of the Chinese Academy of Sciences (Grant No. XDB07020100). Q.M.Z., A.M.Z. and T.L.X were supported by the Fundamental Research Funds for the Central Universities and the Research Funds of Renmin University of China (10XNI038, 14XNLF06, 14XNLQ07). Computational resources have been provided by the Physical Laboratory of High Performance Computing at Renmin University of China. The atomic structures and vibrational displacement patterns were prepared with the XCRYSDEN program [47].

## References:

- [1] S. Kabashima, J. Phys. Soc. Jpn. **21**, 945 (1966).
- [2] E. Revolinsky, J. Appl. Phys. **35**, 2086 (1964).
- [3] M.N. Ali *et al.*, Nature **514**, 205 (2014).
- [4] T. Liang, Q. Gibson, M.N. Ali, M.H. Liu, R.J. Cava, and N.P. Ong, Nat. Mater. **14**, 280 (2015).
- [5] E. Mun, H. Ko, G.J. Miller, G.D. Samolyuk, S.L. Bud'ko, and P.C. Canfield, Phys. Rev. B **85**, 035135 (2012).
- [6] K.F. Wang, D. Graf, L.J. Li, L.M. Wang, and C. Petrovic, Sci. Rep. **4**, 7328 (2014).
- [7] C. Zhang, Z. Yuan, S. Xu, Z. Lin, B. Tong, M.Z. Hasan, J. Wang, C. Zhang, and S. Jia, arXiv:1502.00251.
- [8] P.B. Alers, and R.T. Webber, Phys. Rev. B **91**, 1060 (1953).
- [9] C. Shekhar *et al.*, Nat. Phys. **11**, 645 (2015).
- [10] D.H. Keum *et al.*, Nat. Phys. **11**, 482 (2015).
- [11] I. Pletikoscic, M.N. Ali, A.V. Fedorov, R.J. Cava, and T. Valla, Phys. Rev. Lett. **113**, 216601 (2014).
- [12] J. Jiang *et al.*, Phys. Rev. Lett. **115**, 166601 (2015).

- [13] Y. Wu, N.H. Jo, M. Ochi, L. Huang, D.X. Mou, S.L. Bud'ko, P.C. Canfield, N. Trivedi, R. Arita, and A. Kaminski, *Phys. Rev. Lett.* **115**, 166602 (2015).
- [14] P.L. Cai, J. Hu, L.P. He, J. Pan, X.C. Hong, Z. Zhang, J. Zhang, J. Wei, Z.Q. Mao, and S.Y. Li, *Phys. Rev. Lett.* **115**, 057202 (2015).
- [15] Z.W. Zhu, X. Lin, J. Liu, B. Fauque, Q. Tao, C.L. Yang, Y.G. Shi, and K. Behnia, *Phys. Rev. Lett.* **114**, 176601 (2015).
- [16] Y.K. Luo, H. Li, Y.M. Dai, H. Miao, Y.G. Shi, H. Ding, A.J. Taylor, D.A. Yarotski, R.P. Prasankumar, and J.D. Thompson, *Appl. Phys. Lett.* **107**, 182411 (2015).
- [17] H.Y. Lv, W.J. Lu, D.F. Shao, Y. Liu, S.G. Tan, and Y.P. Sun, *Europhys. Lett.* **110**, 37004 (2015).
- [18] X.C. Pan *et al.*, *Nat. Commun.* **6**, 7805 (2015).
- [19] D.F. Kang *et al.*, *Nat. Commun.* **6**, 7804 (2015).
- [20] Y.P. Qi *et al.*, *Nat. Commun.* **7**, 11038 (2016).
- [21] A.A. Soluyanov, D. Gresch, Z. Wang, Q. Wu, M. Troyer, X. Dai, and B.A. Bernevig, arXiv:1507.01603.
- [22] Y. Sun, S.C. Wu, M.N. Ali, C. Felser, and B.H. Yan, *Phys. Rev. B* **92**, 161107 (2015).
- [23] K.F. Mak, C. Lee, J. Hone, J. Shan, and T.F. Heinz, *Phys. Rev. Lett.* **105**, 136805 (2010).
- [24] T. Boker, R. Severin, A. Muller, C. Janowitz, R. Manzke, D. Voss, P. Kruger, A. Mazur, and J. Pollmann, *Phys. Rev. B* **64**, 235305 (2001).
- [25] J.K. Ellis, M.J. Lucero, and G.E. Scuseria, *Appl. Phys. Lett.* **99**, 261908 (2011).
- [26] R. Dhall, M.R. Neupane, D. Wickramaratne, M. Mecklenburg, Z. Li, C. Moore, R.K. Lake, and S. Cronin, *Adv. Mater.* **27**, 1573 (2015).
- [27] R. Ganatra, and Q. Zhang, *ACS Nano* **8**, 4074 (2014).
- [28] A. Kumar, and P.K. Ahluwalia, *Eur. Phys. J. B* **85**, 186 (2012).
- [29] S.B. Desai, G. Seol, J.S. Kang, H. Fang, C. Battaglia, R. Kapadia, J.W. Ager, J. Guo, and A. Javey, *Nano Lett.* **14**, 4592 (2014).
- [30] W. Liu, W. Cao, J. Kang, and K. Banerjee, *ECS Trans.* **58**, 281 (2013).
- [31] R.K. Ghosh, and S. Mahapatra, *IEEE Journal of the electron devices society* **1**, 175 (2013).
- [32] T. Zandt, H. Dwelk, C. Janowitz, and R. Manzke, *J. Alloys Compd.* **442**, 216 (2007).
- [33] W.G. Dawson, and D.W. Bullett, *Journal of Physics C: Solid State Physics* **20**, 6159 (1987).
- [34] B.E. Brown, *Acta Crystallogr.* **20**, 268–274 (1966).
- [35] C.H. Lee, E. Cruz-Silva, L. Calderin, M.A.T. Nguyen, M.J. Hollander, B. Bersch, T.E. Mallouk, and J.A. Robinson, *Sci. Rep.* **5**, 10013 (2015).
- [36] J. Augustin, V. Eyert, T. Boker, W. Frentrup, H. Dwelk, C. Janowitz, and R. Manzke, *Phys. Rev. B* **62**, 10812 (2000).
- [37] A.C. Ferrari, and D.M. Basko, *Nat. Nanotechnol.* **8**, 235 (2013).
- [38] G. Abstreiter, E. Bauser, A. Fischer, and K. Ploog, *Appl. Phys.* **16**, 345 (1978).
- [39] K.A.N. Duerloo, Y. Li, and E.J. Reed, *Nat. Commun.* **5**, 4214 (2014).
- [40] K.A.N. Duerloo, and E.J. Reed, *ACS Nano* **10**, 289 (2016).
- [41] H.H. Huang, X.F. Fan, D.J. Singh, H. Chen, Q. Jiang, and W.T. Zheng, *Phys. Chem. Chem. Phys.* **18**, 4086-4094 (2016).
- [42] P. E. Blöchl, *Phys. Rev. B* **50**, 17953 (1994); G. Kresse and D. Joubert, *ibid.* **59**, 1758 (1999).
- [43] G. Kresse and J. Hafner, *Phys. Rev. B* **47**, 558 (1993); G. Kresse and J. Furthmüller, *Comp. Mater. Sci.* **6**, 15 (1996); *Phys. Rev. B* **54**, 11169 (1996).
- [44] J. P. Perdew, K. Burke, and M. Ernzerhof, *Phys. Rev. Lett.* **77**, 3865 (1996).

- [45] J. Kliměš, D. R. Bowler, and A. Michaelides, *Phys. Rev. B* **83**, 195131 (2011).
- [46] A. Mar, S. Jobic, and J.A. Ibers, *J. Am. Chem. Soc.* **114**, 8963 (1992).
- [47] A. Kokalj, *Comp. Mater. Sci.* **28**, 155 (2003).